Experimental exploration of compressed beam dynamics in an energy recovery linac with comparison to simulations

Miho Shimada, Norio Nakamura, Tsukasa Miyajima, Yosuke Honda, Takashi Obina, Ryukou Kato, Masafumi Fukuda, Nora P. Norvell, Olga Tanaka, and Hiroshi Sakai

High Energy Accelerator Research Organization, KEK, Oho 1-1, Tsukuba, Ibaraki, Japan and SLAC National Accelerator Laboratory, Menlo Park, California, USA

(Received 28 January 2023; accepted 13 February 2023; published 22 March 2023)

The compact energy recovery linac (cERL) has been developed for industrial applications since 2017. Applications such as free electron laser require a compressed beam with a small energy spread and transverse emittance. The typical operation energy of cERL is an intermediate energy region close to 17.5 MeV; therefore, the electron bunch is easily affected by the longitudinal space-charge effects and the coherent synchrotron radiation wakefield effects. Bunch compression is demonstrated by optimizing a combination of a longitudinally chirped electron bunch and the arcs with nonzero R_{56} parameters. When the bunch compression procedure is applied for a bunch charge of 60 pC, an increase in energy spread is observed at the short bunch length. We systematically explored the chirp phase to determine the best condition. The measurement results of the energy spread, bunch length, and transverse emittance were compared with the tracking simulation results to understand the compressed beam dynamics.

DOI: 10.1103/PhysRevAccelBeams.26.030102

I. INTRODUCTION

The energy recovery linac (ERL) provides a high-quality beam with low emittance, short bunch length, and small energy spread at a high average current at a reasonable operating cost. Such a high-quality electron beam enables a high-intensity free-electron-laser (FEL) or inverse Compton scattering at an undeveloped wavelength region. The electron beam deteriorated due to the light emission process returning its beam power to the accelerating cavity. Subsequently, the return beam power is used for accelerating the fresh and high-quality electron beam from the electron gun. Using such a mechanism, we can effectively extract a bright light from the electron beam.

The ERL accelerators are demonstrated or under consideration at several facilities to develop the new science field and applications due to its aforementioned potential [1–10]. Most ERL projects are based on superconducting linac, making it possible to operate at a high average beam current at a high acceleration gradient. The superconducting linac is used at the European XFEL facility to generate the brilliant x-ray beams despite nonenergy recovery [11], and other XFEL projects are ongoing [12,13]. Therefore, the combination of ERL and the superconducting linac is expected as the most brilliant FEL light source, such as an extreme ultraviolet (EUV) light source for future lithography [14].

In these applications, achieving a high-density electron bunch with a short bunch length and a small transverse beam size is critical. In the typical FEL facility at the higher beam energy, the bunch compression is demonstrated after accelerating more than 100 MeV to achieve a short bunch length with low emittance [15,16]. This is because the electron beams at low-intermediate energy regions (less than 20 MeV) are easily affected by the space-charge effect and coherent synchrotron radiation wakefield (CSR wake) compared with a GeV electron beam [17–21]. The collective effects distort the longitudinal electron distribution and complicate the bunch compression.

As the test of the future EUV-FEL facility, two undulators are installed at the compact ERL (cERL) in the KEK site for demonstration of FEL at the infrared region via a self-amplified spontaneous emission (SASE) FEL process [22]. The SASE-FEL requires a short bunch length with a small energy spread and low transverse emittance to achieve high electron density. In this study, the bunch compression procedure established at an extremely low bunch charge [23,24] was applied for the higher bunch charge of 60 pC.

The cERL is operated at the intermediate energy region, which is around 17.5 MeV. It has long straight sections for

Published by the American Physical Society under the terms of the Creative Commons Attribution 4.0 International license. Further distribution of this work must maintain attribution to the author(s) and the published article's title, journal citation, and DOI.

adding the extra superconducting cavity in the future. Therefore, the longitudinal space-charge (LSC) effect is a serious issue even after full acceleration.

We measured the energy spread and transverse emittance with/without bunch compression to examine the LSC and CSR wake effects. The measurement results were compared with the simulation results. Furthermore, we explored the optimum condition that simultaneously satisfies the short bunch length, small energy spread, and low transverse emittance. We discuss the beam dynamics of the bunch compression at the intermediate energy region by comparing it with the simulation results.

In this article, the chirp phase for longitudinally tilt electron bunch and R_{56} in the arc section were systematically surveyed for the best condition of FEL. The bunch compression is judged with THz-CTR intensity because the two undulators were not completely installed in this experiment. The cERL accelerator and the experimental setup are explained in Secs. II and IV, respectively. The start-to-end tracking simulation and the R_{56} tuning knob are introduced in Sec. III. The calibration of the R_{56} tuning nob and the energy spread measurement result in the bunch compression are shown in Sec. V. Section VI shows the scan results of the chirp phase due to the off-crest acceleration.

II. ACCELERATOR LAYOUT AND MAIN PARAMETERS OF THE CERL

Figures 1 and 2 show the cERL layout and the beam optics used at the beam commissioning. The injector section primarily comprises a high-brightness dc gun, two solenoid magnets, three two-cell superconducting cavities, and five quadrupole magnets. The high-brightness dc gun has a photocathode driven by a pumped laser of 40-ps pulse length. The long bunch length is compressed by the normal conducting buncher cavity's zero-cross acceleration and the first injector cavity's off-crest acceleration. The injection beam merges with the recirculation loop via a dogleg chicane. An electron beam accelerated up to 4–5 MeV is injected into the merger at a 16° injection angle.

The main linac comprises two nine-cell superconducting cavities (ML1 and ML2) modified from the international linear collider cavities for cw operation with high beam current. The electron beams are accelerated up to the full energy (17.5–17.7 MeV) in the recirculation loop. The acceleration gradient of each cavity is determined for stable operation without a field emission. The accelerating phase of the ML1 cavity is on-crest to increase the beam energy as soon as possible whereas that of the ML2 cavity is controlled to make the longitudinal chirp for bunch compression operation.

The straight section, where the main linac is located, is named the north straight section followed by a 180°-arc section. The four bending magnets in the arc section function as the triple bend achromatic optics. The triplet quadrupole magnets between the bending magnet provide a tunable R_{56}, which is the electron's longitudinal drift to the energy deviation. The two undulators (upstream and downstream) were installed at the south straight line in January and May 2020, respectively.

In the study, we report the beam commissioning during the two cases, cases 1 and 2, before the complete installation of the two undulators. The energy ratio between the injector and recirculation loop is limited to 1∶6 in the energy recovery operation, which is determined by the chamber apertures of the injector and dump chicane. However, the injection energy was set to 4–5 MeV in this beam study, whereas the recirculation energy is 17.5–17.7 MeV. The higher injector energy makes it possible to suppress the emittance growth and bunch lengthening due to the space-charge effect. This is because the energy recovery is unnecessary for the bunch compression beam study. Additionally, a minor change was made to the electric dc gun's pumped laser. Table I lists the undulator installation condition and main parameters. The measurement of the collective effects (space-charge effect and CSR wake) was demonstrated in case 2, whereas the longitudinal

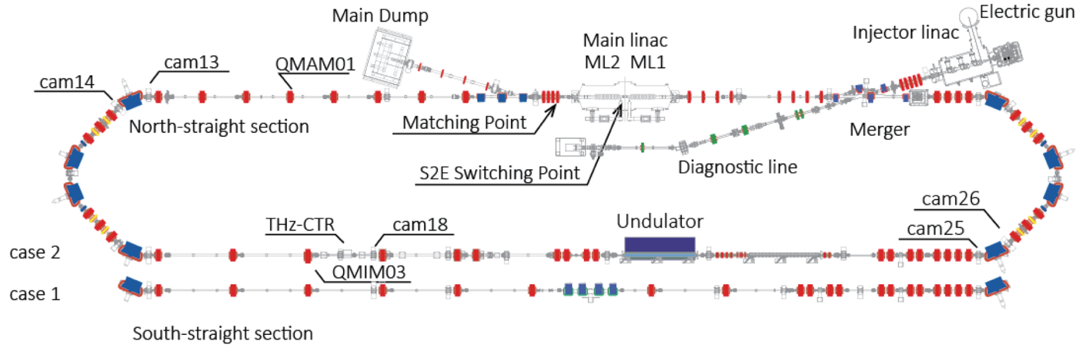

FIG. 1. Schematic layout of the compact ERL of cases 1 and 2.

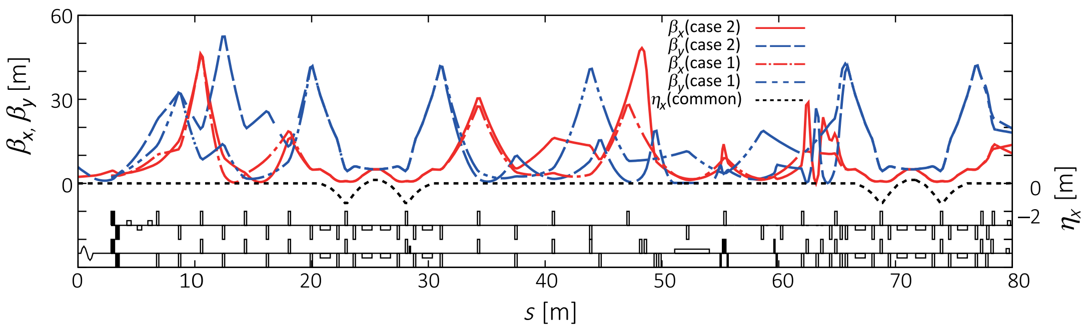

FIG. 2. Beta function β_x, β_y, and dispersion function η_x of isochronous optics. β_x and β_y are minimized using ELEGANT simulation code without the CSR wake and space-charge effects. The positive sign of the x-direction is inside the arc.

chirp's scan study at bunch compression was shown in case 1.

III. BEAM TRACKING SIMULATION FOR BUNCH COMPRESSION

A. Calculation of the space-charge effect and coherent synchrotron radiation wake

The Coulomb force caused by another electron in the same bunch influences electron particles. The LSC effect impedance per unit length in the free space is characterized using the modulation wavelength, λ [25], as follows:

$$Z_{\mathrm{LSC}}(k) = \frac{iZ_0}{\pi k r_b^2}\left[1 - \frac{kr_b}{\gamma} K_1\left(\frac{kr_b}{\gamma}\right)\right] \tag{1}$$

where $k = 2\pi/\lambda$ is the wave number, $Z_0 = 377\Omega$ is the free space impedance, r_b is the transverse cross-section radius, K_1 is the modified Bessel function, and γ is the relativistic factor. The LSC effect increases the energy spread and lengthening of the bunch length even after full acceleration at the cERL because of the intermediate energy region. The head (tail) of the electron bunch gains (losses) its energy by the LSC effect. It modifies the energy spread and the longitudinal chirp of the entire electron bunch and limits the bunch compression for FEL operations [26].

TABLE I. Main operation parameters of the compact ERL and condition of the undulator installation.

Case	Case 1	Case 2
Beam energy of injection beam (MeV)	4	5
Beam energy of recirculation beam (MeV)	17.5	17.7
rf frequency (GHz)	1.3	1.3
Repetition frequency of micropulse (MHz)	1300	81.25
Repetition frequency of macropulse (Hz)	5	5
Bunch charge (pC)	60	60
Pulse stacking of gun laser	Yes	No
Undulator	None	One

The envelope equation of the rms transverse beam size, σ, is written as the following equation of the orbital position, s [27,28]:

$$\frac{\sigma}{\mathrm{d}s^2} + k(s)\sigma = \frac{\varepsilon^2}{\sigma^3} + \frac{K_{sc}}{\gamma^3\sigma}, \tag{2}$$

where ε and $k(s)$ are the transverse emittance and external force, respectively. The beam perveance $K_{sc} = I_p/2I_A$, where I_p and I_A are the peak current and Alfvén current, respectively (approximately 17 kA). The second term on the right-hand side is sufficiently larger than the first term of the bunch compression's typical parameters at the cERL recirculation loop. The transverse emittance growth due to the space charge is estimated with the numerical tracking simulation.

CSR wake also increases the energy spread and horizontal emittance. This is caused by the bunch's tail radiation field catching up with the head of the same bunch moving along a curved orbit [29–31]. The coherent radiation emitted by the short electron bunch has a shorter wavelength and causes more energy loss. The energy loss gradient is written as follows:

$$\frac{\mathrm{d}E(s)}{\mathrm{d}s} = -\frac{2Ne^2}{\sqrt{2\pi}3^{1/3}\rho^{2/3}\sigma_z^{4/3}} F_0(s/\sigma_z) \tag{3}$$

$$F_0(x) = \int_{-\infty}^{x} \frac{\mathrm{d}x'}{(x-x')^{1/3}} \frac{\partial}{\partial x'} \exp(-x'^2/2) \tag{4}$$

where ρ is the bending radius, e is the electron charge, and N is the number of electrons in the bunch. The longitudinal bunch distribution is assumed as the Gaussian shape at the rms size of σ_z. The longitudinal energy distribution is distorted by the energy loss (gain) based on s in the bending magnet. It induces the emittance growth in the horizontal direction. In this study, the tracking simulation of CSR wake was performed by the solution [32,33], which is derived from Jefimenko's form of Maxwell's equation rather than Liénard Wiechert formulas. This makes it possible to directly calculate the coherent electromagnetic field using the evolving charge and current densities. Although it is approximated into a one-dimensional (1D) model in the longitudinal direction, it provides a more realistic solution compared with other 1D model simulations (e.g., ELEGANT [34]) that overestimate the wakefield at lower energy electron bunch. The shielding effect is negligible in the cERL because the bending magnet's curvature radius is 1 m, which is small for a few ps bunch lengths.

The numerical tracking simulation, including the space-charge effect and CSR wake, is demonstrated by General Particle Tracer (GPT) [35,36]. The 3D space-charge field is calculated by solving Poisson's equation in the bunch's rest frame on a nonuniform mesh. The CSR wake simulation is demonstrated with the aforementioned 1D model. The equation of motion for the macroparticles is solved relativistically using the particle-in-cell methods in the time domain. The electrical forces acting on the electron are simulated at each time step; thus, the electron motion is self-consistent.

B. Magnetic bunch compression with off-crest acceleration

To avoid the strong space-charge effect and CSR wake at the low beam energy, the bunch compression is conducted after full acceleration to maintain a small emittance in both transverse and longitudinal directions. The ML2 cavity's off-crest acceleration provides the energy chirp on the electron bunch. The chirped bunch transports the following arc section with nonzero R_{56} and T_{566}, which are defined as follows:

$$\Delta z = R_{56}\Delta E/E_0 + T_{566}(\Delta E/E_0)^2 + \cdots, \qquad (5)$$

where z is the longitudinal position in the electron bunch and $\Delta E/E_0$ is the energy deviation divided by the nominal electron energy E_0. The sign of R_{56} is negative in a typical arc section when the positive z means the head in the electron bunch. The parameter of R_{56} is described as $R_{56} = \int \eta_x(s)/\rho(s)\mathrm{d}s$, where η_x is the horizontal dispersion function.

The arc sections are the quasitriple bend achromat lattice for easily tuning R_{56} [24,37]. When the dispersion function is symmetric through the arc section, R_{56} at the cERL can be written as $R_{56} = 2\eta_c \sin\theta + 4\rho(\theta - \sin\theta)$, where θ and η_c are the bending angle and the dispersion function at the center of the arc section, respectively. The arc section is composed of four 45° bending magnets instead of three to measure η_c. Figure 3 shows the arc section's lattice layout and dispersion function.

The quadrupoles in the arc section are used only to control R_{56} while maintaining the achromat condition. If the LSC effect is negligible, the optimum R_{56} for minimum bunch length is $k_{\mathrm{rf}} \sin\phi_{\mathrm{rf}} = 1/R_{56}$, where k_{rf} is the wave number of the rf accelerating cavity and ϕ_{rf} is the off-crest phase. However, the energy chirp is modified by the LSC effect before arriving at the arc section and the optimum R_{56} shifts from the linear approximated equation. Two sextupole magnets (SXs) were settled at the large dispersion function in the arc section. The magnets are mainly used to control T_{566} for correcting the longitudinal phase space's quadratic distortion, which is affected by the curvature of the 1.3-GHz rf cavity.

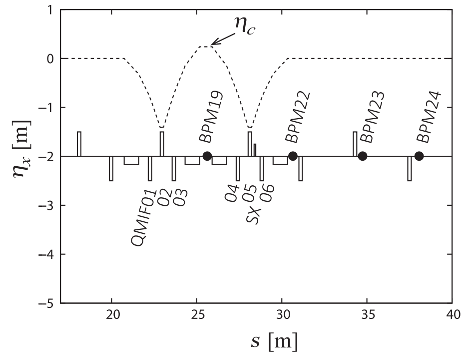

FIG. 3. Example of dispersion function η_x of the arc section with the lattice layout and positions of BPMs.

C. Optics design and tracking simulation for beam tuning

The beam optics is designed separately, i.e., the start-to-end (S2E) simulation, at the switching point between ML1 and ML2 of the main linac (Fig. 1). At the low-energy region before entering the ML2 cavity, compressing the transverse emittance growth due to the space-charge effect is the most important issue. Therefore, it is optimized using the genetic algorithm based on the tracking results of GPT to maintain low emittance [38] and fixed during one experiment season. The CSR wake effect is excluded to minimize calculation time because the electron energy is too low to emit synchrotron radiation at the bending magnets in the THz region. The north straight section is used for optics matching to the recirculation loop at every beam study season.

The accelerating phases of ML2 and R_{56} of the arc section are explored for the bunch compression tuning after the beam optics at the low-energy region are fixed. The R_{56} tuning knob is expressed by the change in the focus strength of the quadrupole magnets $K[\mathrm{m}^{-1}]$, ΔK. The ratio of ΔK of QMIF01 : QMIF02 : QMIF03 is about - 1 : 2 : 0, which is obtained from the design of linear optics. The ratio is constant within the typical tuning range of R_{56}. The ratio is selected to keep the achromat condition and the beta function almost constant during the R_{56} tuning. The linear optics is maintained close to symmetric even during the R_{56} scan to estimate the R_{56} value from the measured dispersion function η_c.

The optics of the recirculation loop is calculated using the ELEGANT simulation code from the switching point. The arc section is used only to control the dispersion function for the longitudinal beam distribution, while the two straight sections to the betatron function for the transverse beam distribution. The optics in Fig. 2 shows the isochronous condition. Estimating the impact of the space-charge effects and CSR wake at the recirculation loop was demonstrated by the GPT-tracking simulations. Then, the tracking simulation results were compared with the experimental results in this study.

IV. EXPERIMENTAL SETUPS FOR BEAM DIAGNOSTICS

A. Measurements of the dispersion function

A beam position monitor (BPM) is used to measure the transverse beam position from the reference orbit. The strip-line BPM signal is filtered at 1.3 GHz, which is the beam repetition rate. The beam position's accuracy was calibrated with the nearest screen monitor, and the jitter is smaller than 200 μm. The dispersion function is obtained from the beam position shift by reducing the recirculation beam energy by 1%.

B. Bunch length estimation

A deflecting cavity is a strong tool for measuring the bunch length after completing the bunch compression; however, it was not installed in the recirculation loop to avoid causing beam instability due to the high average beam current. Therefore, the bunch length is estimated from the coherent transition radiation (CTR) from the aluminum-coated Si plate at the THz region [23]. The plate can be removed at a high average current operation. The THz-CTR is focused on the bolometer detector with several parabola aluminum mirrors on the optical bench. The detector's sensitivity range is 150 GHz–20 THz.

C. Energy spread measurement

The energy spread is estimated from the horizontal beam size at the Ce:Yag screen monitors settled in a nonzero dispersion area in the arc section. The measurement resolutions, which depend on the screen monitors, are about 50 μm. Figure 1 shows the locations of the energy spread measurement. The energy spread after off-crest acceleration is measured at the screen monitor, cam14. The design value of the dispersion function is 0.49 m, whereas the experimental value is 0.52 m. Although the horizontal beam size on the screen monitor was minimized at every measurement in this study, the measurement accuracy was approximately 10% due to the effect of the betatron function and transverse emittance. A screen monitor, cam26, was used the same way as cam14 after bunch compression.

D. Transverse emittance measurements

The transverse emittance is measured using the Q scan method, in which an upstream quadrupole magnet was used to scan the rms beam size. The measurements are investigated at the north and south straight sections, which are dispersion free, to compare the emittance before and after bunch compression. The quadrupole magnet, QMAM01, is used at the north straight section to satisfy the thin lens approximation. Other quadrupole magnets located between QMAM01 and screen monitor cam13, are degaussed during the Q-scan measurement. Furthermore, the combination of QMIM03 and cam18 is selected at the south straight section. Figure 1 shows the location of the quadrupole magnet and screen monitor.

V. PROCEDURE AND MEASUREMENT RESULTS OF THE BUNCH COMPRESSION

A. R_{56} tuning of the achromat arc

The longitudinal dispersion function R_{56} of the whole arc section is estimated from the horizontal dispersion function η_c at the center of the arc, as described in the previous section. In this method, the optics of the arc section should be achromat and symmetric. Both R_{56} and η_c are estimated from the dispersion function at BPM19, whereas the achromat condition is verified using two of the three BPMs in the south straight section, BPM22, BPM23, and BPM24. The BPM positions are shown in Fig. 3. Just setting the focus strength of the design optics, the arc section does not satisfy the achromat condition due to unknown errors. To minimize leakage of the dispersion function into the south straight section, QMIF01 and QMIF06 are tuned by the same amount of ΔK, which are sensitive to the achromat condition. Additionally, the SXs with additional correct coils are used as a skew magnet to suppress unexpected vertical dispersion.

After finding the achromat condition, we experimentally survey the R_{56} tuning knob, which also has a discrepancy between the design value and experimental results. The proper ratio of ΔK of QMIF01 : QMIF02 : QMIF03 was 1 : 1.7 : 0 based on the experimental results. The tuning knob is slightly affected by the condition of the injector beam distribution because the dispersion function measured at the high bunch charge is sensitive to the gun laser pulse shape and the longitudinal beam distribution. Therefore the best ratio is surveyed at every commissioning season. The tuning knob makes it possible to scan R_{56} within a few minutes by maintaining small leakage of the dispersion function.

The dispersion functions of the arc section simulated using the two codes, ELEGANT and GPT, are shown in the left graph of Fig. 4, which contains no collective effect of the space-charge effect and CSR wake. Despite a slight discrepancy between the simulation codes, the dispersion function at BPM19 changes linearly with R_{56}, whereas the other BPMs are close to zero. The right-hand graph shows the experimental results. It is obtained by the 60-pC bunch

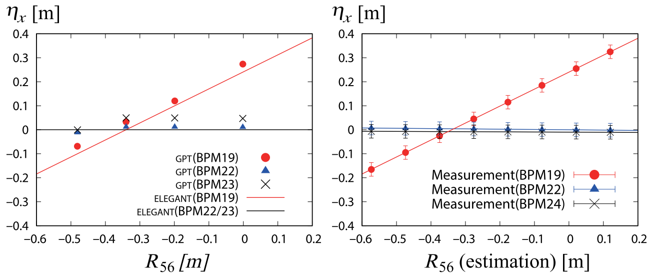

FIG. 4. Horizontal dispersion function η_x of the arc section during R_{56} scan. Left: results from ELEGANT are compared with those from GPT-tracking simulation. Right: results of experimental measurements.

charge, in which the space-charge and CSR wake effects are non-negligible. Although the achromat condition appears to be slightly broken, the behaviors of the BPMs are similar to the simulation.

B. Off-crest acceleration and chirp phase

To express the off-crest acceleration, we define the chirp phase by the acceleration phase of ML2, which can be independently controlled. The longitudinal bunch distribution is already tilted at the exit of the main linac and further modified due to the LSC effect in the north straight section even at full acceleration. Therefore, the on-crest acceleration phase for maximizing energy gain does not correspond to the minimum energy spread.

The longitudinal tilt at the arc entrance is critical for bunch compression. The zero chirp phase is defined as the minimum energy spread at the arc entrance. The tracking simulation results are summarized at several chirp phases, as shown in Fig. 5. The central beam energy at every chirp phase was tuned to 17.7 MeV by the accelerating field of ML2. The accelerating field was minimum at the 25° chirp phase of (d) in Fig. 5, which means the on-crest acceleration. The phase space of (d) was tilted at cam13 because it is already tilted before the injection of the main linac. Furthermore, the longitudinal distribution is bent because the core part with high electron density is more tilted by the LSC effect than the other surrounding electrons at the north straight section after full acceleration. The bent affects the longitudinal distribution after bunch compression.

At the beam commissioning, the central beam energy is measured using cam14 at the nonzero dispersion region of the arc entrance. The energy spread $\sigma_{\Delta E/E_0}$ and the rms horizontal beam size σ_x are obtained by fitting the Gaussian function to the beam distribution projected to the horizontal axis. The experimental results of $\sigma_{\Delta E/E_0}$, σ_x, and the accelerating field of ML2 were compared with the tracking results in Fig. 6.

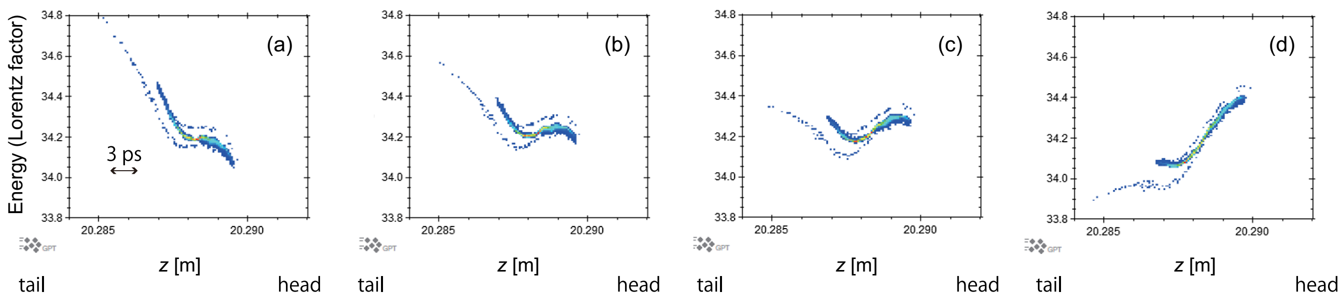

FIG. 5. GPT-tracking results of the longitudinal distribution at cam13 at several chirp phases of ML2 cavity. The + 0° chirp phase is at the minimum energy spread at the arc entrance. (a) −8°, (b) +0°, (c) +8°, and (d) +25° (the on-crest acceleration). The positive value of the z-axis is the traveling direction.

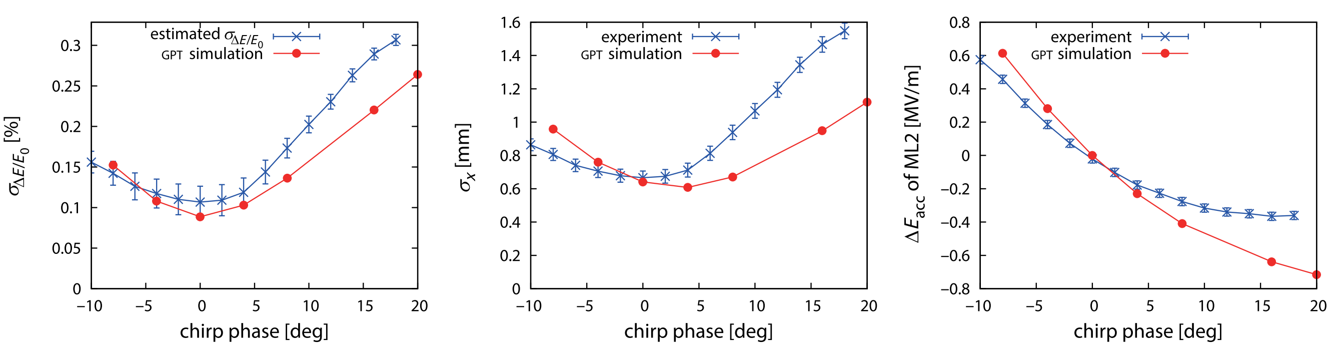

FIG. 6. Left: beam energy spread estimated from the rms horizontal beam size at cam14 and GPT-tracking simulation results. Center: experimental and GPT simulation results of the rms horizontal beam size. Right: shift of accelerating gradient E_{acc} of the cavity ML2 to maintain the beam energy of 17.7 MeV at off-crest acceleration.

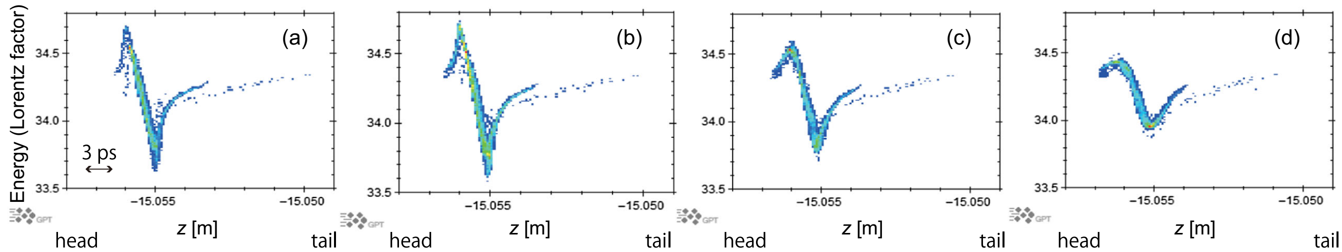

FIG. 7. GPT-tracking results of the longitudinal distribution at cam25 at the chirp phase of $+8°$. R_{56} of the arc section are (a) −0.34 m, (b) −0.27 m at the minimum bunch length at THz-CTR, (c) −0.2 m, (d) −0.13 m, respectively. The smaller z means the bunch head contrary to Fig. 5 at the north straight section (cam13).

In the left graph, $\sigma_{\Delta E/E_0}$ was estimated from σ_x, which is not simply proportional to $\sigma_{\Delta E/E_0}$ and includes the effects of the betatron function β_x and normalized horizontal emittance ε_{nx} as follows $\sigma_x = \sqrt{\eta_x^2(\Delta E/E_0)^2 + \beta_x \varepsilon_{nx}/\gamma}$. The second term depends on the chirp phase because the injection beam with a non-Gaussian transverse profile feels the different focusing force of the superconducting cavity [39]. According to the simulation results in the center graph, the chirp phase of the minimum $\sigma_{\Delta E/E_0}$ was different from that of σ_x by 3–4 degrees. Therefore, the zero chirp phase purposely defined at the minimum $\sigma_{\Delta x}$ in the experimental results has an error of a few degrees. The right graph shows the accelerating field, in which the error bar comes from the energy tuning at cam14.

The acceleration field was minimum at the chirp phase of 17° in the experimental results but was 25° in the simulation results. The discrepancy between the simulation and experimental results was larger than the error bars even at the arc entrance. This indicates that the precise prediction of the longitudinal phase space is challenging.

C. Energy spread measurement after bunch compression

Figure 7 shows the simulation results of the longitudinal distribution at cam25, which is the dispersionless region and is close to cam26. Because of the bunch compression, the longitudinal distribution is complicatedly bent and has a long tail, and the energy spread depends on the R_{56}. The left graph of Fig. 8 shows the tracking simulation results during the R_{56} scan: the rms bunch length at the THz-CTR measurement location and the energy spread at cam26. The energy spread was maximized when the bunch length was minimized. This is because the CSR wake and LSC effects are enhanced at the shorter bunch length. CSR wake induces energy loss contrary to the LSC effect. According to the tracking simulation, this induces energy loss less than 0.01%, which is smaller than the beam energy's measurement resolution.

To measure the energy spread and center energy shift after bunch compression, the electron beam is transported to the nonzero dispersion, which is the entrance of the return arc (cam26). The LSC effect continues through the south straight section, whereas the CSR wake occurs only in the bending magnet. Although the electron beam travels through the undulator in case 2, there was no significant beam loss and the effect on this beam study was negligible.

The energy spread and center shift estimated from the rms horizontal beam size and position after bunch compression are compared to the THz-CTR intensity in Fig. 8. The THz-CTR intensity during the R_{56} scan exhibits a large peak indicating that the whole bunch length is minimized by the bunch compression procedure, instead of the enhancement of the longitudinal microbunch structure. Therefore, the bunch compression was judged by the THz-CTR intensity. We found that the horizontal beam size exhibits a large peak at the maximum THz-CTR intensity. The peak in the horizontal beam size is larger than that in the vertical one, which is dispersionless. On the other hand, the center position is slightly shifted at the

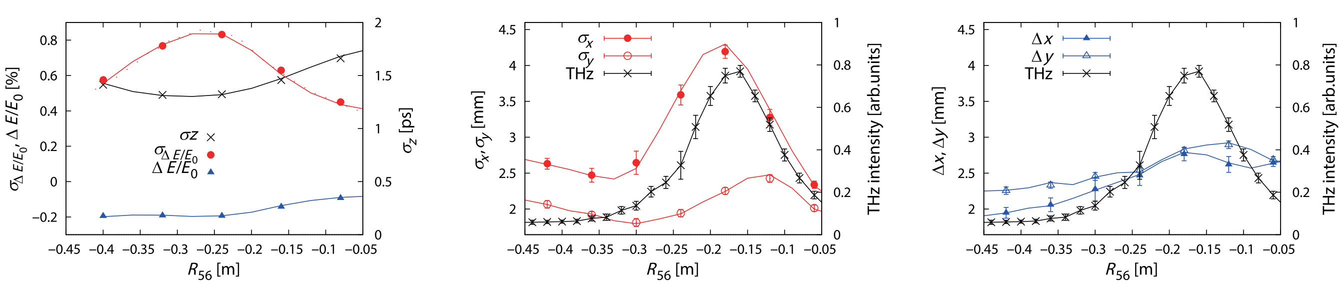

FIG. 8. Energy spread $\sigma_{\Delta E/E_0}$ and bunch length σ_z at cam26 during R_{56} scan. Left: GPT-simulation results. Center: measurement results of rms beam size. Right: beam center position.

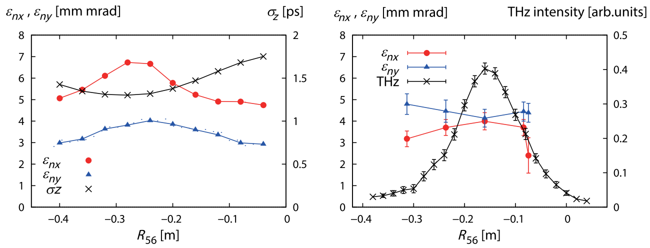

FIG. 9. Transverse emittances ε_x, ε_y at cam18 during R_{56} scan. Left: GPT-simulation results. Right: measurement results.

maximum THz-CTR intensity, and the horizontal shift is comparable to that of the vertical one.

The transverse emittances were measured at the exit of the arc section (cam18) at several R_{56}. The measurements are compared with the tracking simulation results (Fig. 9). In the tracking simulation, horizontal and vertical emittance slightly increase at the short bunch length. For experimental results, the error bars are larger than the changes despite the horizontal emittance slightly increased at the maximum THz-CTR intensity.

VI. SURVEY OF CHIRP PHASE AT BUNCH COMPRESSION

The bunch compression optimization was demonstrated at several chirp phases. The tuning knob of R_{56} is used to optimize the linear optics, and the SX is used to correct the quadric deformation on the longitudinal distribution. The beam orbit is carefully centered at the SX to avoid changing the linear optics, achromat condition, and R_{56}, at the off-center in the SX. Scans of R_{56} and SX are iterated to find the maximum THz-CTR intensity.

In the same way as Sec. V, the energy spread was measured at cam14 and cam26 before and after bunch compression, respectively. Figure 10 summarizes the results. The experimental results were compared with the tracking simulation results calculated in the same parameter setup, in which the rms bunch length was minimized.

The optimized values of R_{56} at the chirp phases of $-8°$ and $+8°$ were 0.49 and -0.05 m for the experimental results and 0.34 m and -0.31 m for the simulation results, respectively. Although the experimental results differ from the simulation results, the difference in R_{56} between the chirp phases of $-8°$ and $+8°$ is almost 0.6 m in both cases. On the other hand, there was no regularity of the SX's optimum strength in both experimental and simulation results.

The THz-CTR intensity used to judge the bunch compression in the experiment was large at the positive large chirp phase. Although the energy spread was already relatively large due to the positive large chirp phase acceleration even before the bunch compression, we discovered a significant increase in the energy spread after bunch compression. In the simulation results, the bunch length was short, and the energy spread was large, indicating that the bunch compression was successful, and the bunch length was compressed shorter at the large chirp phase, as described in Sec. III B. The simulation results show that the horizontal emittance at each chirp phase slightly increases. On the other hand, in the experimental results at the chirp phase of $+8°$, the horizontal emittance before bunch compression was already larger

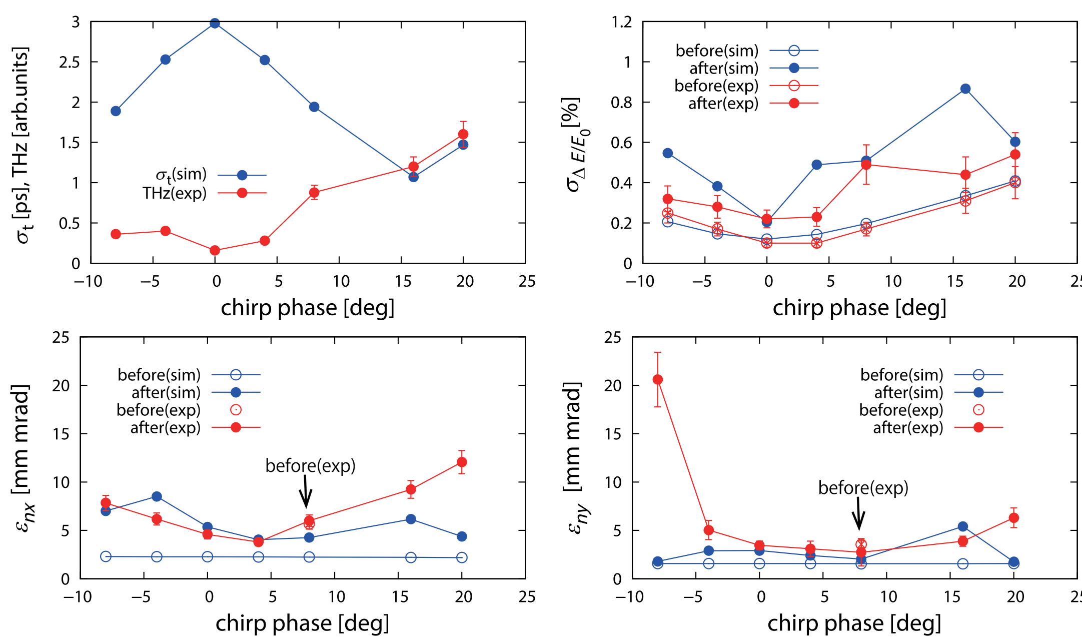

FIG. 10. Comparison between experimental and simulation results of the main beam parameters at case 1 before/after bunch compression at the several chirp phase of ML2. Transverse emittances before bunch compression are measured at only $+8°$.

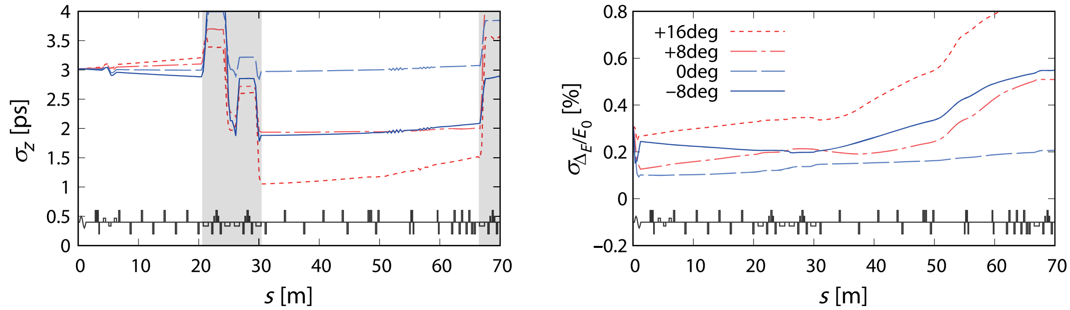

FIG. 11. GPT-simulation results of the bunch length σ_z and energy spread $\sigma_{\Delta E/E_0}$ at the several chirp phase of Fig. 10. The direction of z is defined as the same direction at the exit of the main linac; therefore, σ_z in the arc section (gray zone) does not correspond to the bunch length. Locations of THz-CTR measurement and cam26 are at $s = 35.7$ m and $s = 67.8$ m, respectively.

than that in the simulation results. The horizontal emittance and energy spread gradually increased at the larger chirp phase; therefore, the chirp scan was terminated at $+20°$.

Regarding the negative chirp, the THz-CTR intensity was smaller than that of the positive chirp phase, and the increase in the energy spread was smaller than in the positive chirp. It means the bunch compression does not work well. The vertical emittance drastically increased at the chirp phase of $-8°$; however, it did not appear in the tracking simulation. It is why the chirp scan was terminated at $-8°$.

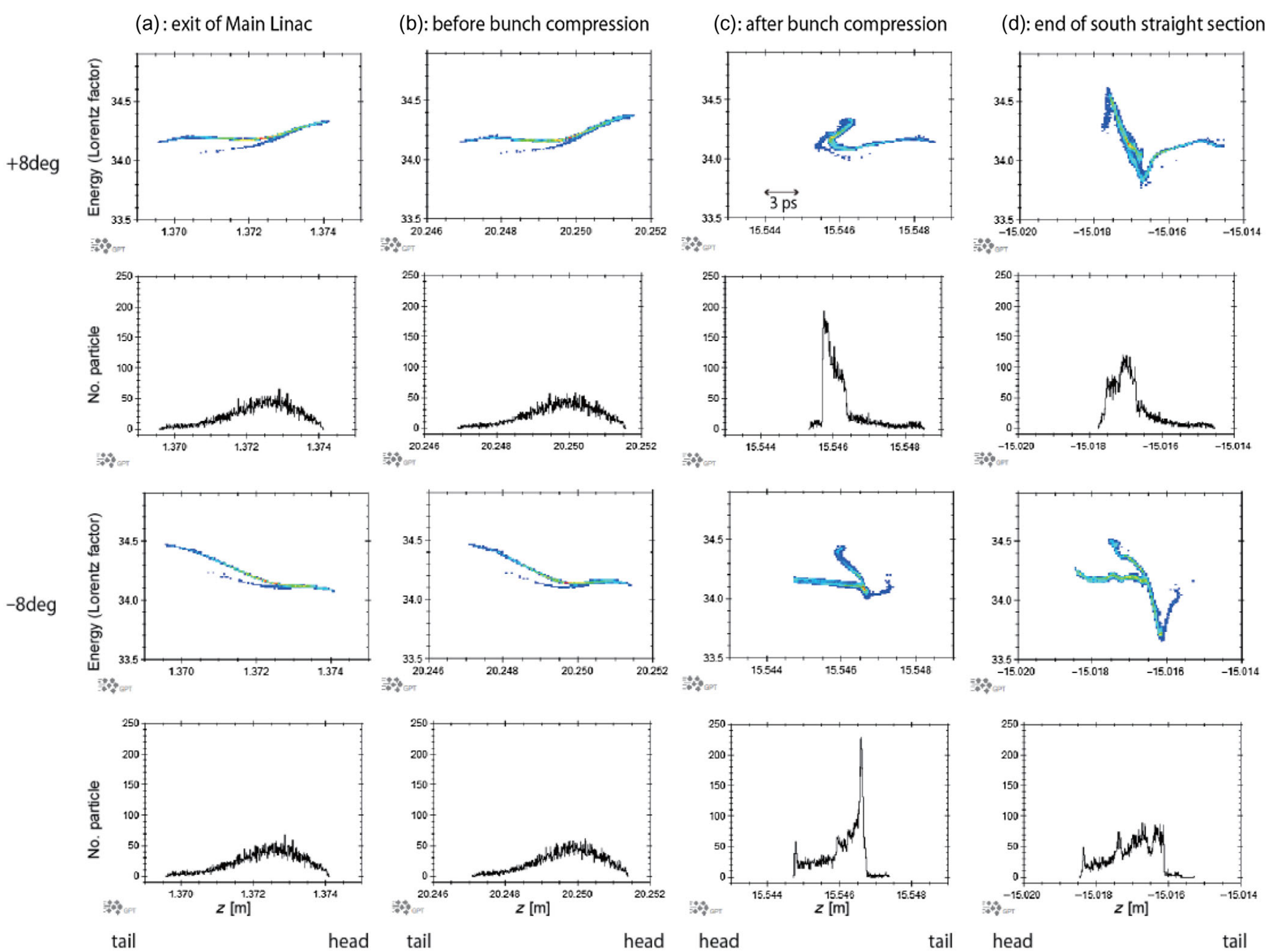

FIG. 12. Longitudinal phase space distribution and histogram at the chirp phases of $+8°$ and $-8°$. The locations in Fig. 1 are (a) exit of the main linac, (b) cam13, (c) THz-CTR, and (d) cam26, respectively. The definition of the z direction is reversed after passing through the 180-degree-arc section.

Figure 11 shows the simulation results of the rms bunch length σ_z and energy spread $\sigma_{\Delta E/E_0}$ during the bunch compression. The energy spread increased larger at the smaller bunch length after bunch compression. Although the bunch lengths at the chirp phase of $+8°$ and $-8°$ were almost the same, the energy spread at the south straight section ($30 \text{ m} < z < 67 \text{ m}$) was slightly small at $+8°$. The LSC effect at the north straight section before the arc section ($z < 20$ m) enhanced the energy spread at $+8°$ but suppressed it at $-8°$. On the other hand, the energy spread was compressed at $+8°$ in the arc section ($20 \text{ m} < z < 30 \text{ m}$) but was enhanced at $-8°$ due to the LSC or CSR wake effect. At the middle of the south straight section ($z > 40$ m), the energy spread increased at both chirp phases of $\pm 8°$.

The longitudinal distribution illustrated in Fig. 12 was slightly tilted between (a) and (b) due to the LSC effect in the north straight section. After the arc section (c), the compressed bunch was accompanied by a long tail in both cases of $+8°$ and $-8°$. The core part with high-density electrons feels the strong space-charge effects; therefore, the increase in the energy spread appeared partially at the core part after the south straight section (d). In the case of $-8°$, the complicated longitudinal distribution at the exit of the main linac was enhanced due to the bunch compression.

Based on the experimental results of case 1, the chirp phase of $+8°$ is considered the best for the FEL experiment, requiring a short bunch length, small energy spread, and small transverse emittance. The chirp phase scan is demonstrated at each operation season because the optimum chirp phase is sensitive to the accelerator condition, setup, and the surrounding environment.

VII. DISCUSSIONS

The procedure of bunch compression was applied for the bunch charge of 60 pC for FEL demonstration. The main parameters were the arc section's chirp phase and R_{56}. The bunch compression tuning was optimized for the maximum THz-CTR intensity. The energy spread was measured at the entrance of the return arc section, which is about 20 m downstream from the location of the THz-CTR measurement.

The beam optics and transport matrix of the real machine slightly differed from that of the design used in the optics calculation and the tracking simulation. Therefore, we need some calibrations. The parameter of the R_{56} tuning knob was calibrated based on the BPM measurements, making it possible to scan R_{56} with maintaining the achromatic condition. Thanks to the R_{56} scan tool, we can find the best R_{56} for the real beam distribution as shown in Fig. 4.

There are two reasons for the discrepancy in the optimum value of R_{56} between the simulation and experimental results in Fig. 10. First, the energy spread before bunch compression was estimated from the horizontal beam size measured at cam14. According to the simulation result in Fig. 6, the minimum energy spread differed by a few degrees from that of the horizontal beam size. Therefore, the definition of the chirp phase was slightly different from the minimum energy spread. Another reason is that the longitudinal distribution has a discrepancy between the real beam and simulation results at the switching point of the start-to-end simulation. The curves of the accelerating field of ML2 to the chirp phase in the left graph in Fig. 6 did not agree with each other. However, the differences in the optimum R_{56} between $+8°$ and $-8°$ are 0.5–0.6 m, which are almost the same. Therefore, although the absolute value of R_{56} was uncertain, the tuning of R_{56} was successful for each chirp phase.

At the R_{56} scan shown in Fig. 8, we observed that the energy spread increases after bunch compression at the shorter bunch length, which is estimated at the THz-CTR intensity. However, the energy shift was negligible because the changes in the center beam occur even in the dispersionless vertical direction. The small position changes occurred in the Gaussian fitting error of the distorted distributions. Therefore, the energy spread is assumed to occur by the LSC effect, which is not accompanied by energy loss, rather than the CSR wake. The same surmise is derived from the tracking simulation in Fig. 11, which shows the energy spread increases at the south straight section. According to Fig. 9, the horizontal emittance is slightly increased at the bunch compression in both measurement and simulation. However, the emittance has large error bars; therefore, the relationship between the bunch length and emittance is unclear. The vertical emittance also slightly increased at the short bunch length in the simulation; however, the experimental result is already large regardless of the bunch compression.

Figure 10 summarizes the chirp phase scan. At the positive large chirp phase, the THz-CTR intensity and energy spread are large, which is the same as the tracking simulation. As described in Sec. III B, it is a reasonable result showing that the bunch length after the bunch compression is shorter at the larger chirp phase. For the IR-FEL, the chirp phase around $+8°$ was best because the energy spread increases at the large chirp phase. The large vertical emittance at the large negative chirp can be explained as the effect of SX. According to other tracking simulations, it grows when the beam passes through the SX with an off-center orbit or large betatron function. The large amplitude of ML2 in Fig. 6 can distort the vertical orbit and betatron function. The increase in the energy spread in the experiment is smaller than that in the simulation results. It is considered that the bunch length was not compressed down to that in the tracking simulation.

The LSC effect modifies the longitudinal distribution at the intermediate energy. At the north straight section before bunch compression, the longitudinal tilt was enhanced by the LSC effect at the positive chirp phase, in which the bunch head has the higher energy, as shown in Fig. 11. The negative chirp was compensated. Therefore, the acceleration field of ML2 should be increased to maintain the recirculation beam energy (Fig. 6) and the negative chirp. The change of the accelerating field can induce the distortion of the orbit and betatron function downstream. On the other hand, the energy spread decreased at $+8°$ in the 30 m $< z < 40$ m at the exit of the arc section because the higher energy electrons go back to the bunch tail in the negative R_{56} arc section, and the LSC effect compensated the longitudinal bunch tilt. However, the LSC effect after bunch compression was stronger than before and the energy spread increases due to the strong LSC effect at $z > 40$ m. Concerning the chirp phase of $-8°$, the energy spread turned to increase from the arc section. Therefore, the energy spread at $-8°$ was slightly larger than at $+8°$ despite the minimum bunch length being almost the same. The compensation occurred even in the longitudinal distribution far from the Gaussian profile, as shown in Fig. 12. The tracking simulations also clarify that the LSC effect increases the energy spread at the high-density core part in the south straight section after bunch compression. In the experiment, the bunch compression was not successful at the negative chirp according to the small THz-CTR intensity. It can be caused by the beam profile distortion by the high acceleration field of ML2.

VIII. CONCLUSION

One of the goals of the cERL is for application usages, such as FEL. The bunch compression was experimentally explored at the intermediate energy region and compared with the tracking simulation results. The tuning knob for R_{56} is calibrated in the bunch compression procedure because the real magnet response is slightly different from the design one. The bunch compression is experimentally judged by the increase in CTR-THz intensity, and the energy spread also increases. According to the tracking simulation, the energy spread is caused in the straight section after bunch compression, indicating that the LSC effect, rather than CSR wake, is dominant in the arc section. The best chirp phase controlled by the accelerator cavity is explored to obtain both short bunch length and small energy spread, simultaneously. The bunch compression was experimentally successful at a positive energy chirp phase but not a negative chirp. The LSC effects compensate for the energy chirp at the negative chirp; therefore, it needs a higher acceleration field and sometimes induces optics distortion and emittance growth. On the other hand, the LSC effect enhances a positive chirp phase and suppresses the energy spread during bunch compression. Therefore, the positive chirp phase is suitable for bunch compression under the strong LSC effects. We selected the chirp phase of $+8°$ for cERL at the commissioning season of case 1. The operation parameters, the injection beam profile, and the procedure of the optics tuning are established.

ACKNOWLEDGMENTS

We express our appreciation for the fruitful discussion about the beam dynamics of the bunch compression with Dr. R. Hajima (QST) and the hardware and beam operation support of Dr. M. Yamamoto and Dr. N. Higashi (KEK). Part of the experiments are demonstrated under the financial support of the New Energy and Industrial Technology Development Organization (NEDO) project "Development of advanced laser processing with intelligence based on high-brightness and high-efficiency laser technologies (TACMI project)." and JSPS KAKENHI Grant No. JP18H03473.

[1] A. Bartnik *et al.*, CBETA: First Multipass Superconducting Linear Accelerator with Energy Recovery, Phys. Rev. Lett. **125**, 044803 (2020).

[2] M. Amold *et al.*, First ERL operation of S-DALINAC and commissioning of a path length adjustment system, in *Proceedings of the 9th International Particle Accelerator Conference, IPAC2018, Vancouver, BC, Canada* (JACoW, Geneva, Switzerland, 2018), pp. 4859–4862.

[3] M. Abo-Bakr *et al.*, The Berlin energy recovery linac project BERLinPro - status, plans and future opportunities, in *Proceedings of the 63th ICFA Advanced Beam Dynamics Workshop on Energy Recovery Linacs (ERL'19), Berlin, Germany* (JACoW Publishing, Geneva, Switzerland, 2019), paper MOCOXBS04, 10.18429/JACoW-ERL2019-MOCOXBS04.

[4] I. Ben-Zvi, Superconducting energy recovery linacs, Supercond. Sci. Technol. **29**, 103002 (2016).

[5] R. Hajima, Energy recovery linacs for light sources, Rev. Accel. Sci. Technol. **03**, 121 (2010).

[6] G. R. Neil *et al.*, Sustained Kilowatt Lasing in a Free-Electron Laser with Same-Cell Energy Recovery, Phys. Rev. Lett. **84**, 662 (2000).

[7] V. Borin *et al.*, Measurements of beam parameters at the last track of ERL-based Novosibirsk Free Electron Laser, in *Proceedings of the 10th International Particle Accelerator Conference, IPAC-2019, Melbourne, Australia* (JACoW, Geneva, Switzerland, 2019), pp. 2632–2634.

[8] N. R. Thompson *et al.*, Status of the ALICE IR-FEL: From ERL Demonstrator to User Facility, in *Proceedings of the 37th International Free Electron Laser Conference FEL2015, Daejeon, Korea* (JACoW, Geneva, Switzerland, 2015), pp. 379–383.

[9] R. Hajima, T. Shizuma, M. Sawamura, R. Nagai, N. Nishimori, N. Kikuzawa, and E. J. Minehara, First demonstration of energy-recovery operation in the JAERI superconducting linac for a high-power free-electron laser, Nucl. Instrum. Methods Phys. Res., Sect. A **507**, 115 (2003).

[10] M. Akemoto *et al.*, Construction and commissioning of the compact energy-recovery linac at KEK, Nucl. Instrum. Methods Phys. Res., Sect. A **877**, 197 (2018).

[11] The European x-ray free-electron laser technical design report, DESY, Hamburg, Report No. DESY-06-097, 2007, 10.3204/DESY_06-097.

[12] Linac Coherent light source II (LCLS-II) conceptual design report, SLAC National Accelerator Laboratory, Menlo Park, CA, Report No. SLAC-R-978, 10.2172/1029479.
[13] J. Yan and H. Deng, Multi-beam-energy operation for the continuous-wave x-ray free electron laser, Phys. Rev. Accel. Beams, **22**, 090701 (2019).
[14] H. Kawata, N. Nakamura, H. Sakai, R. Kato, and R. Hajima, High power light source for future extreme ultraviolet lithography based on energy-recovery linac free-electron laser, J. Micro/Nanopatterning, Mater., Metrol., **21**, 021210 (2022).
[15] C. C. Hall, S. G. Biedron, A. L. Edelen, S. V. Milton, S. Benson, D. Douglas, R. Li, C. D. Tennant, and B. E. Carlsten , Measurement and simulation of the impact of coherent synchrotron radiation on the Jefferson Laboratory energy recovery linac electron beam, Phys. Rev. ST Accel. Beams **18**, 030706 (2015).
[16] Y. Ding *et al.*, Measurement and Simulations of Ultralow Emittance and Ultrashort Electron Beams in the Linac Coherent Light Source, Phys. Rev. Lett. **102**, 254801 (2009).
[17] T. Miyajima *et al.*, 60 pC Bunch charge operation of the compact ERL at KEK, in *Proceedings of the 8th International Particle Accelerator Conference, IPAC-2017, Copenhagen, Denmark* (JACoW, Geneva, Switzerland, 2017), pp. 890–893.
[18] C. Gulliford *et al.*, Demonstration of low emittance in the Cornell energy recovery linac injector prototype, Phys. Rev. ST Accel. Beams, **16**, 073401 (2013).
[19] B. Muratori *et al.*, Space charge effect for the ERL prototype at Daresbury Laboratory, in *Proceedings of the 9th European Particle Accelerator Conference, Lucerne, 2004* (EPS-AG, Lucerne, 2004), pp. 446–448.
[20] M. Shimada *et al.*, Systematic measurements of the coherent THz spectra by magnetic bunch compression at the compact ERL, in *Proceedings of the 10th International Particle Accelerator Conference, IPAC-2019, Melbourne, Australia* (JACoW, Geneva, Switzerland, 2019), pp. 1486–1488.
[21] A. He, F. Willeke, L. H. Yu, L. Yan, T. Shaftan, G. Wang, Y. Li, Y. Hidaka, and J. Qiang, Design of low energy bunch compressors with space charge effects, Phys. Rev. ST Accel. Beams **18**, 014201 (2015).
[22] Y. Honda *et al.*, Construction and commissioning of mid-infrared self-amplified spontaneous emission free-electron laser at compact energy recovery linac, Rev. Sci. Instrum. **92**, 113101 (2021).
[23] Y. Honda, M. Shimada, T. Miyajima, T. Hotei, N. Nakamura, R. Kato, T. Obina, R. Takai, K. Harada, and A. Ueda , Beam tuning and bunch length measurement in the bunch compression operation at the cERL, Nucl. Instrum. Methods Phys. Res., Sect. A **875**, 156 (2017).
[24] M. Shimada *et al.*, Bunch compression at the recirculation loop of compact ERL, in *Proceedings of the 7th International Particle Accelerator Conference, IPAC-2016, Busan, Korea* (JACoW, Geneva, Switzerland, 2016), pp. 3008–3010.
[25] Z. Huang, M. Borland, P. Emma, J. Wu, C. Limborg, G. Stupakov, and J. Welch, Suppression of microbunching instability in the linac coherent light source, Phys. Rev. ST Accel. Beams **7**, 074401 (2004).
[26] A. Khan, O. Boine-Frankenheim, F. Hug, and C. Stoll, Beam matching with space charge in energy recovery linacs, Nucl. Instrum. Methods Phys. Res., Sect. A **948**, 162822 (2019).
[27] M. Ferrario, M. Migliorati, and L. Palumbo, Space charge effects, in *Proceedings of the CAS-CERN Accelerator School*, edited by W. Herr (CERN, Geneva, Report No. CERN-2014-009, 2014).
[28] T. P. Wangler, *RF Linear Accelerators* (John Wiley & Sons, Inc., New York, 2008), Chap. 9, ISBN 0-471-16814-9.
[29] J. B. Murphy *et al.*, Longitudinal wakefield for an electron moving on a circular orbit, Part. Accel. **57**, 9 (1997).
[30] Ya. S. Derbenev, J. Rossbach, E. L. Saldin, and V. D. Shiltsev, Microbunch radiative tail-head interaction, Report No. TESLA-FEL 95-05, 1995.
[31] D. Sagan, G. Hoffstaetter, C. Mayes, and U. Sae-Ueng, Extended one-dimensional method for coherent synchrotron radiation including shielding, Phys. Rev. ST Accel. Beams **12**, 040703 (2009).
[32] I. V. Bazarov and T. Miyajima, Calculation of coherent synchrotron radiation in General Particle Tracer, in *Proceedings of the 11th European Particle Accelerator Conference, Genoa, 2008* (EPS-AG, Genoa, Italy, 2008), pp. 118–120.
[33] C. Mayes and G. Hoffstaetter, Exact 1D model for coherent synchrotron radiation with shielding and bunch compression, Phys. Rev. ST Accel. Beams **12**, 024401 (2009).
[34] M. Borland, Elegant, https://www.aps.anl.gov/Accelerator-Operations-Physics/Software.
[35] General Particle Tracer (GPT) code, Pulsar Physics, http://www.pulsar.nl/gpt/.
[36] J. Qiang, R. D. Ryne, S. Habib, and V. Decyk, An object-oriented parallel particle-in-cell code for beam dynamics simulation in linear accelerators, J. Comput. Phys. **163**, 434 (2000).
[37] F. Jackson, D. Angal-Kalinin, Y. M. Saveliev, P. H. Williams, and A. Wolski, Longitudinal transport measurements in an energy recovery accelerator with triple bend achromat arcs, Phys. Rev. Accel. Beams **19**, 120701 (2016).
[38] T. Miyajima *et al.*, Status of higher bunch charge operation in compact ERL, in *Proceedings of the 6th International Particle Accelerator Conference, IPAC-2015, Richmond, VA* (JACoW, Geneva, Switzerland, 2015), pp. 1583–1586.
[39] J. Rosenzweig and L. Serafini, Transverse particle motion in radio-frequency linear accelerators, Phys. Rev. E **49**, 1599 (1994).